



Contents lists available at SciVerse ScienceDirect

Electrochimica Acta

journal homepage: www.elsevier.com/locate/electacta



Conversion mechanism of nickel fluoride and NiO-doped nickel fluoride in Li ion batteries

Dae Hoe Lee^a, Kyler J. Carroll^a, Scott Calvin^b, Sungho Jin^a, Ying Shirley Meng^{a,*}

^a Department of NanoEngineering, University of California San Diego, 9500 Gilman Drive, La Jolla, CA 92093, USA

^b Department of Physics, Sarah Lawrence College, Bronxville, NY 10708, USA

ARTICLE INFO

Article history:

Received 19 July 2011

Received in revised form 15 October 2011

Accepted 20 October 2011

Available online xxx

Keywords:

Conversion mechanism

Nickel fluoride

NiO-doped nickel fluoride

Nucleation and growth of Ni

Superparamagnetism

ABSTRACT

The conversion mechanism of NiF₂ and NiO-doped NiF₂ during electrochemical cycling was investigated using a combination of structural analysis by ex situ X-ray diffraction (XRD), X-ray photoelectron spectroscopy (XPS), X-ray absorption spectroscopy (XAS) and magnetic analysis by superconducting quantum interference device (SQUID) magnetometry. It was observed that the conversion reactions in both cathode materials were partially reversible; however, they differ in their conversion rate. NiO-doped NiF₂ exhibited enhanced electrochemical properties in terms of the conversion potential and reversibility due to the presence of a NiO phase, which has slightly higher electronic conductivity than NiF₂. It is suggested that the NiO doping reduced the nucleation sites for Ni nanoparticles, subsequently enhancing the kinetics of the conversion reaction involving the growth of Ni particles formed during lithiation. The ex situ XRD and the magnetic hysteresis data (H_C and M_S) indicate that the average dimension of the Ni particles formed along with LiF in pristine NiF₂ and NiO-doped NiF₂ during the 1st lithiation was in the superparamagnetic regime, with 4–5 nm and 8–9 nm particle sizes, respectively. Although the particle size was decreased to the nanoscale, the original NiF₂ phase was regenerated by re-lithiation.

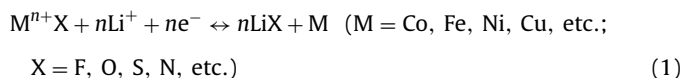
© 2011 Elsevier Ltd. All rights reserved.

1. Introduction

The lithium ion battery is one of the most important rechargeable energy storage devices, since it has a high energy density, long cycle life, high working cell potential and reliable safety. Lithium ion batteries are also one of the leading candidates for the power sources in electric vehicles. Although the performance of lithium ion batteries has been improving rapidly in recent years, there are still several issues that need to be resolved for applications requiring higher energy density.

Choosing the best cathode material used in a Li-ion battery is one of the most crucial issues in achieving higher energy densities, since the energy density is directly correlated to the specific capacity associated with that cathode material [1]. The intercalation-based materials, such as LiFePO₄, LiMn₂O₄, and LiCoO₂ with specific capacities ranging from 100 to 150 mA h g⁻¹ are widely utilized as the positive electrode of commercial Li-ion batteries. These materials exhibit excellent cycling properties since the structure of the cathode materials are not significantly changed during the intercalation and de-intercalation of lithium ions [2]. The intercalation-based materials, however, yield only a limited spe-

cific capacity because of the structure and corresponding restricted valence changes of the transition metals. This insufficiency can be overcome by utilizing conversion based cathode materials that tend to exhibit substantially higher capacities, due to the fact that essentially all the possible oxidation states of the compound during the redox reaction can be utilized [3]. The overall conversion reaction can be summarized as the following:



The conversion type materials have been studied as potential electrode materials for high energy lithium ion batteries. Tarascon's group first demonstrated that these conversion materials, which were Co₃O₄, CoO, NiO, and FeO, can exhibit high specific capacities of 600–1000 mA h g⁻¹ along with good cycling properties [3–5]. However, these metal oxides are only suitable for use as negative electrodes, due to their low conversion potential, which is lower than 1.0 V.

Transition metal fluorides have recently been investigated as potential cathode materials because of their high electronegativity [6–9]. However, the insulating nature of metal fluorides has limited their electrochemical properties for a long time; for that reason a considerable amount of attention has been devoted by Badway et al. [10–12], to tailoring their nanostructures to overcome poor

* Corresponding author. Tel.: +1 8588224247; fax: +1 8585349553.
E-mail address: shmeng@ucsd.edu (Y.S. Meng).

electronic conductivity. It has been demonstrated that nanocomposites of carbon and metal fluorides such as FeF_2 , FeF_3 , and BiF_3 may be utilized as cathodes for next generation high energy lithium ion batteries, revealing a high conversion potential and good cycling properties [10,11,13,14]. In addition, the metal fluoride compounds including M–O covalent bond such as FeOF and Fe_2OF_4 have been reported to exhibit better electrochemical properties, since M–O bond provides higher electronic conductivity into highly insulating M–F ionic bond [15,16]. However there are very few studies on NiF_2 based conversion cathode materials in terms of the conversion mechanism and electrochemical properties, due to its poor electrochemical properties compared to other metal fluorides [17].

In this study, we focused on the investigation of the conversion mechanisms during discharge and charge in NiF_2 and NiO-doped NiF_2 at room temperature. NiO doping was attempted with an aim to improve electronic conductivity by introducing covalent M–O bonds [18,19]. The structure of NiO-doped NiF_2 was investigated by XRD, XPS and XAS analysis. Ex situ XRD was conducted to study the structural changes during the conversion reactions in both NiF_2 and NiO-doped NiF_2 . In order to understand the phases formed by the conversion reactions more thoroughly, we utilized a SQUID magnetometer, which is a powerful technique for detecting nanosized magnetic particles such as Ni nanoparticles that otherwise could be missed by diffraction based analytical techniques.

2. Experimental

2.1. Materials preparation

Commercially available NiF_2 (Alfa Aesar) powder was used for this study. Subsequently the NiF_2 was annealed at 500°C for 1 h under the atmosphere of a mixture of argon and partial air to dope the NiO phase.

2.2. X-ray diffraction (XRD)

XRD patterns were collected using a Rigaku Multiflex diffractometer with $\text{Cu K}\alpha$ radiation by scanning each sample in the 2θ range of 20 – 80° at a rate of 0.02°s^{-1} . In order to take ex situ XRD, lithiated and delithiated electrochemical cells were disassembled in an Ar-filled glovebox and the cathode electrodes were washed with acetonitrile (Alfa Aesar) 3 times. The dried electrodes were placed on a glass slide, covered with Kapton film and sealed with a layer of vacuum grease around the perimeter in the glovebox to reduce moisture and/or oxygen contamination. XRD data analysis was carried out by utilizing Rietveld refinement using the FullProf software package [20].

2.3. X-ray photoelectron spectroscopy (XPS)

XPS measurements were carried out using a Thermo Scientific K-alpha spectrometer using a monochromatic $\text{Al K}\alpha$ (1486.6 eV) X-ray source. Charge compensation was also utilized during analysis and all data was charge shifted to the aliphatic C 1s hydrocarbon. Prior to analysis, the powdered samples were pressed onto a strip of double-sided adhesive tape.

2.4. Magnetic characterization

SQUID measurements were done with a quantum design physical property measurement system (PPMS). The magnetic hysteresis loops were obtained at both at 5 K and 300 K over the field range of -20 kOe to 20 kOe, and the magnetic susceptibility was measured at -20 kOe from 5 K to 300 K.

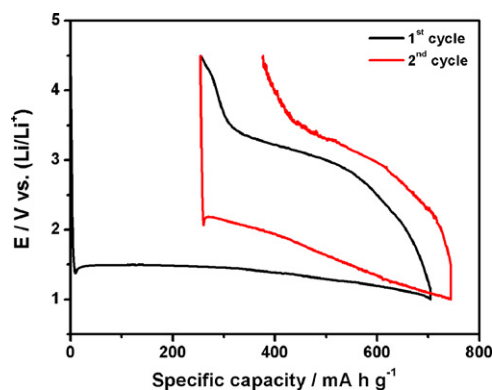


Fig. 1. Electrochemical profiles for NiF_2 from the 1st discharge to 2nd discharge, performed at room temperature at 16.15 mA g^{-1} .

2.5. X-ray absorption spectroscopy (XAS)

Extended X-ray absorption fine-structure spectroscopy (EXAFS) spectra were collected at beamline 4-1 of the Stanford Synchrotron Radiation Lightsource (SSRL), utilizing a silicon (220) double-crystal monochromator detuned approximately 30% as well as a harmonic rejection mirror. Transmission spectra at the Ni K edge were collected along with a simultaneous spectrum on a reference foil of metallic nickel to assure consistent energy calibration. Data were analyzed using the Iffeffit [21] and Horae [22] packages.

2.6. Electrochemical characterization

Electrochemical characterization was performed using coin-type (2016) cells. The working electrodes were composed of either NiF_2 or NiO-doped NiF_2 , carbon black (Super-P), and polyvinylidene fluoride (PVDF) at a weight ratio of 10:10:8 respectively. Pure lithium metal was used as a counter electrode. The coin cells were assembled with the electrolyte consisting of 1 M LiPF_6 dissolved in ethylene carbonate (EC) and dimethylene carbonate (DMC) with a volume ratio of 1:1 (Novolyte), and polypropylene separators (Celgard) in an MBraun Ar-filled glovebox ($\text{H}_2\text{O} < 0.1$ ppm). Electrochemical cycling was performed using a battery cycler (Arbin) at room temperature, with a constant current density of 16.15 mA g^{-1} , and a cell potential range of 1.0–4.5 V.

3. Results

3.1. Electrochemical properties of NiF_2

As shown in Fig. 1, the electrochemical performance of the NiF_2 electrodes were investigated in the cell potential range of 1.0–4.5 V at room temperature at a 16.15 mA g^{-1} rate. Pristine NiF_2 exhibited greater than 700 mA h g^{-1} at the 1st discharge by a conversion reaction involving the reduction of Ni^{2+} to Ni^0 (Eq. (1)). The specific capacity is somewhat higher than the theoretical specific capacity by $\sim 150\text{ mA h g}^{-1}$. This overcapacity is ascribed to the contribution from side reactions such as the formation of solid electrolyte interface (SEI) layer during the lithiation, since the operating cell potential is lower than 1.5 V. A slow cell potential drop was observed after the 200 mA h g^{-1} at the 1st discharge, indicating that the side reactions are possibly proceeding from the early stages of conversion reaction. It has been proposed by other researchers that a significantly increased surface area is formed since nanosized metal particles are produced as a consequence of the conversion reaction [9–14]. Therefore, a significant amount of SEI layer can be formed during the conversion reaction [3–5]. In the 1st charge, $63.5\% \pm 1\%$ of discharged capacity was converted back

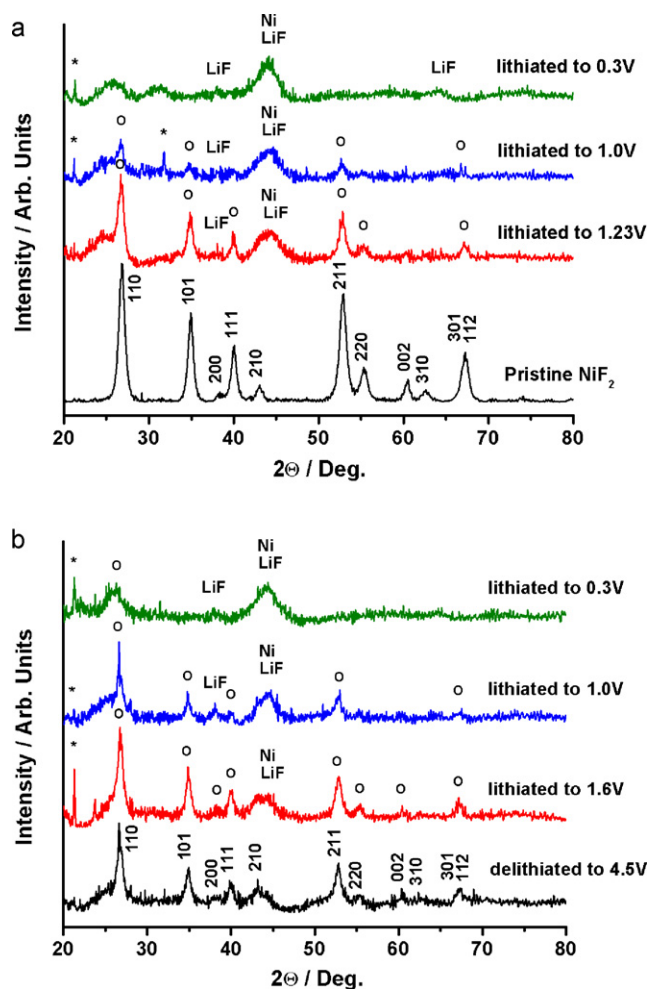


Fig. 2. Ex situ XRD patterns for the (a) 1st lithiation and (b) 2nd lithiation in pristine NiF_2 . (°) Reflections are assigned to NiF_2 and (*) marks impurities related to Li_2CO_3 .

(recovered), indicating that this reaction is reversible. However, the irreversible capacity was still significant due to the formation of the SEI layer and an incomplete conversion reaction. We will discuss this phenomenon in more detail later with the magnetic data. The theoretical conversion potential of NiF_2 is 2.964 V [7]. However, the measured conversion potential was only 1.5 V, which is 1.464 V lower than the theoretical conversion potential due to the highly insulating nature of M–F ionic bonding, the slow rate of nucleation and growth of M/LiX and the structural reconstruction during the conversion process [10–14].

3.2. Structural changes in NiF_2 during the conversion reaction by XRD

Fig. 2(a) shows the XRD patterns of the 1st discharged NiF_2 samples. The Bragg reflections assigned to NiF_2 became weaker in intensity with increasing lithiation. Simultaneously the reflections corresponding to Ni and LiF were developed, indicating that a two-phase conversion reaction involving the nucleation and growth of Ni particles was occurring. The Ni and LiF phases were detected from the early stages of the conversion reaction at 1.23 V and their signals became more intense and sharper with the lithiation, since the nucleation and growth of Ni particles proceeded with the conversion process. The NiF_2 phase was still observed at ~1.0 V and it disappeared completely at 0.3 V, indicating that the conversion reaction was essentially terminated and proceeded extremely slowly. The Bragg reflections of the NiF_2 were significantly

broadened with lithiation, since NiF_2 particles became nanocrystalline. Although the higher capacities, 875 mA h g^{-1} and 800 mA h g^{-1} for the NiF_2 and NiO-doped NiF_2 respectively, were obtained upon 0.3 V lithiation, a lower cut-off voltage (1.0 V) was used due to poor reversibility, presumably from the formation of irreversible side reactions with the electrolyte that occur under 1.0 V. The crystallite sizes of Ni particles after the 1st discharge and the 2nd discharge, estimated from the Scherrer equation using the most intense (1 1 1) Bragg peak, were around 4 nm and 3.5 nm, respectively. This crystallite size is similar to the size regime of Fe particles converted from another conversion compound system FeF_3 [23].

Fig. 2(b) shows the XRD patterns from the 1st charge and during the 2nd discharge. The NiF_2 phase was regenerated after the 1st charge and there were no corresponding peaks to Ni and LiF, indicating that the conversion reaction is a reversible process. However, all of the Bragg reflections were broad and weak, and no strong crystalline phases were detected, which is hypothesized to originate from the line-broadening caused by the formation of nanosized particles. The electrochemical charge and discharge processes are extremely slow, which in a sense could be viewed to be in a pseudo thermodynamic equilibrium; therefore the broadening due to strain should be insignificant. The conversion mechanism in the 2nd discharge appears to be the same as in the 1st discharge. The reflections corresponding to Ni and LiF were observed from 1.6 V and their signals became larger and sharper with continued lithiation due to the growth of the Ni phase. We will show later in magnetic measurements that in fact the size of the Ni particles are very different in the 2nd discharge compared with that in the 1st discharge.

Based on the ex situ XRD experiment, the conversion reaction in NiF_2 appeared to be an essentially reversible process, however, the electrochemical reversibility at the 1st cycle was only $63.5\% \pm 1\%$. In order to acquire a better understanding of the conversion mechanisms involved in the formation of the nanosized-particles and irreversibility of the reaction, we conducted magnetic measurements using a SQUID magnetometer.

3.3. Magnetic properties of NiF_2 during the conversion reaction

Temperature- and field-dependent magnetizations of the lithiated and delithiated samples were acquired to assess the superparamagnetic behaviors of nanosized Ni particles, and magnetic hysteresis (H_C and M_S). Both measurements were performed after zero-field cooling (ZFC). The magnetization (in units of emu g^{-1}) intensity is based on the mass of NiF_2 for the initial and 1st charged samples, and the mass of Ni for the 1st and 2nd discharged samples. At the blocking temperature (T_B), the ferromagnetic moment within each nanoparticle decouples from the crystal lattice and becomes superparamagnetic. For dc SQUID measurements, T_B is typically expressed as $T_B = KV/(25 k_B)$, such that the magnetocrystalline anisotropy energy (KV) is much greater than thermal energy, where V is the ferromagnetic particle volume. Therefore T_B decreases with decreasing particle size. For $T > T_B$, the particle rapidly achieves thermal equilibrium during the measurement time and the system behaves as a superparamagnet. On the other hand, the magnetic moments remain at a fixed direction during a single measurement when $T < T_B$. The temperature dependent magnetization of Ni nanoparticles shows a hysteresis below T_B [24,25].

As shown in Fig. 3(a), pristine NiF_2 is antiferromagnetic material, which has the Néel temperature T_N (the temperature above which an antiferromagnetic material becomes paramagnetic) at 60 K. After the 1st discharge to 1.0 V, NiF_2 showed superparamagnetic behavior since the NiF_2 was mostly converted to nanosized-Ni particles and LiF. Since nanosized-Ni particles achieve thermal equilibrium during the measurement time due to their extremely

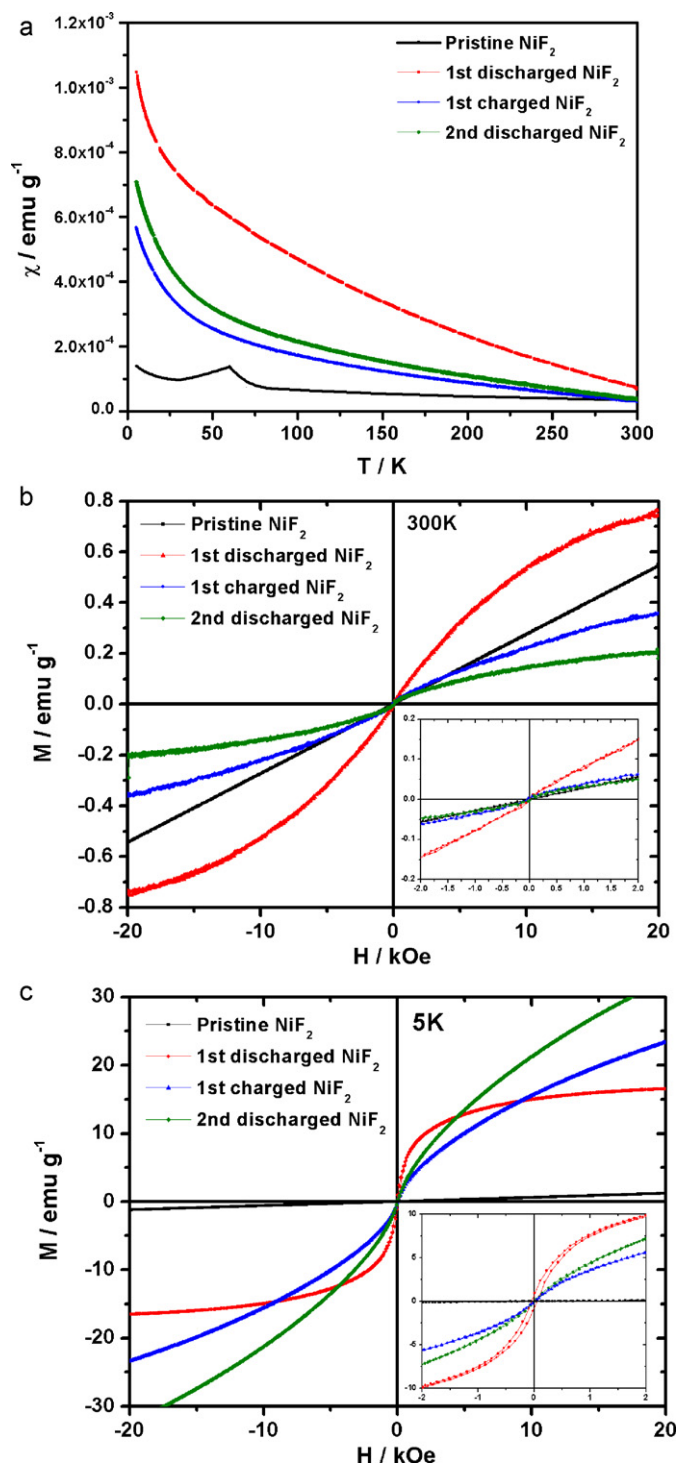


Fig. 3. Magnetic properties for pristine, 1st discharged, 1st charged, and 2nd discharged NiF_2 by SQUID. (a) Magnetic susceptibilities according to the temperature, (b) magnetic hysteresis loops against the magnetic field (-20 to 20 kOe) at 300 K, and (c) at 5 K. The insets correspond to enlargements of hysteresis loop between -2 kOe and 2 kOe.

small size, T_B was not found even cooling down to 5 K. According to the previous study by Johnston-Peck et al. [26] T_B was not found even at 2.5 K in the 2.8 nm Ni particles. The magnetic behavior was not recovered to the antiferromagnetic state after the 1st charge, even though NiF_2 phase was clearly observed by XRD (Fig. 2(b)). We believe that there is a certain amount of unreacted nanosized-Ni particles in the regenerated NiF_2 after the 1st charge,

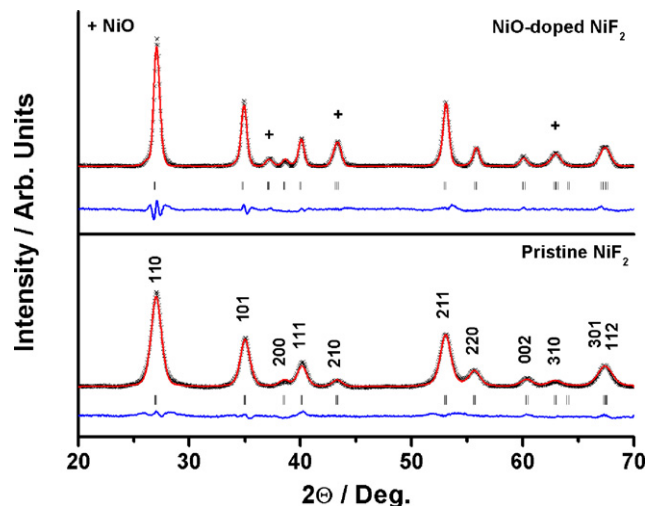


Fig. 4. XRD patterns of pristine NiF_2 and NiO-doped NiF_2 including a Rietveld refinement. (hkl) Marks the Bragg diffractions related to NiF_2 .

revealing that the reversibility of the conversion reaction is not 100%.

Fig. 3(b) and (c) shows the magnetic hysteresis loops against the applied magnetic field. As shown in Fig. 3(b), all samples exhibited negligible hysteresis at 300 K, which indicates that the particles became superparamagnet near room temperature. (The Curie temperature of bulk Ni is 633 K.) This is because the NiF_2 was mostly converted to nanosized-Ni particles by the conversion reaction. It is also suggested that the conversion reaction in NiF_2 is very slow, which contributes to the formation of extremely small particles. As shown in Fig. 3(c), the 1st discharged NiF_2 exhibited noticeable magnetic hysteresis at 5 K, implying that the nanosized-Ni particles formed were small enough to decrease T_B to around 5 K. These magnetic measurements were consistent with the results of ex situ XRD and gave us the confidence that the nanosized metal particles are indeed generated by the conversion reaction. The superparamagnetism was also observed in the 1st charged NiF_2 , since there is still unreacted Ni in the phase, which was not detected clearly by XRD.

3.4. Structure of NiO-doped NiF_2 by XRD, XPS and XAS

NiO doping into NiF_2 was conducted for the purpose of improved electrochemical properties by introducing covalent M–O bonds into highly ionic M–F bonds. Rietveld refinements of the X-ray patterns, especially two-phase refinements for the NiO-doped NiF_2 , were performed using the Fullprof Suite software [20]. The refined parameters and conventional Rietveld R-factors are presented in Table 1. As shown in Fig. 4, the NiO doping was performed by annealing at 500°C under the atmosphere of argon and air mixture. It was suspected whether the Ni–O–F phase was formed by the annealing. In the earlier research on iron oxyfluoride by Pereira et al., a lattice parameter was decreased by 0.15 Å after the Fe–O–F was formed [16]. However, a lattice parameter of NiO-doped NiF_2 was decreased only by 0.025 Å and increased by 0.0035 Å in c lattice parameter, which is too slight to consider that Ni–O–F phase was formed by the annealing. There was no significant change in atomic positions, and occupancies as well. Therefore, we concluded that only the NiO phase was formed in the NiF_2 as a consequence of the annealing in the oxygen-containing atmosphere. On the basis of two-phase refinement analysis, it is estimated that ~ 14.6 wt% of NiO phase was doped on the NiF_2 after the annealing. The peaks corresponding to NiF_2 appeared to be sharper in NiO-doped NiF_2 , indicating that the crystallinity was improved or the particle size

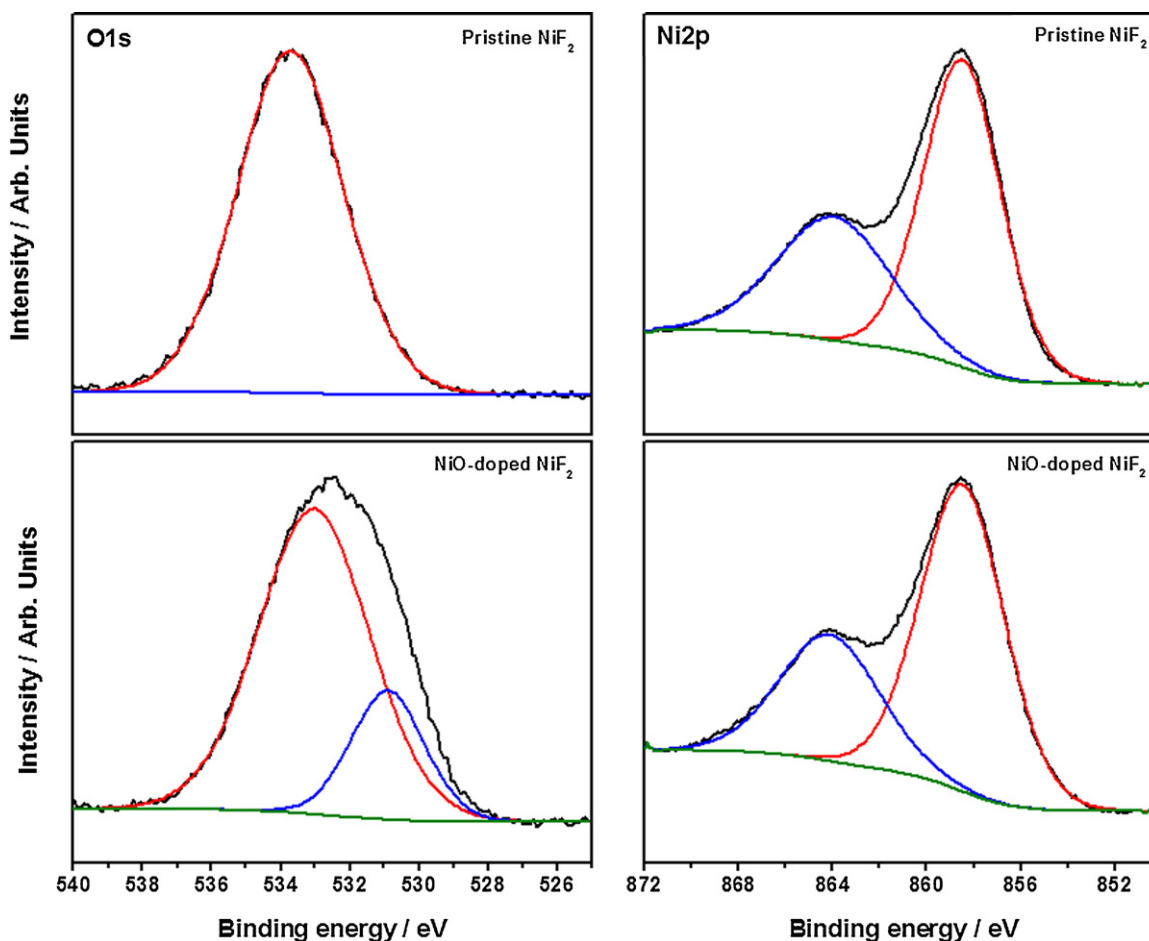
Table 1
Parameters and reliability factors obtained by the Rietveld refinement of the pristine NiF₂ and NiO-doped NiF₂ XRD diffraction patterns.

Pristine NiF ₂ space group: P 42/m n m						NiO-doped NiF ₂ space group: P 42/m n m					
Atom	Site	X	Y	z	Occ.	Atom	Site	x	y	z	Occ.
Ni	2a	0	0	0	1	Ni	2a	0	0	0	1
F	4f	0.302(7)	0.302(7)	0	2	F	4f	0.300(8)	0.300(8)	0	2
$a = b = 4.6675(6) \text{ \AA}$, $c = 3.0632(9) \text{ \AA}$ $R_{\text{wp}} = 2.26\%$, $R_{\text{B}} = 8.22\%$						$a = b = 4.6421(5) \text{ \AA}$, $c = 3.0667(2) \text{ \AA}$ $R_{\text{wp}} = 2.39\%$, $R_{\text{B}} = 5.61\%$					
NiO space group: F d -3 m											
Atom	Site	x	y	z	Occ.						
Ni	4a	0	0	0	1						
O	4b	0.5	0.5	0.5	1						
$a = b = c = 4.1648(9) \text{ \AA}$ $R_{\text{wp}} = 2.39\%$, $R_{\text{B}} = 7.19\%$											
Mass fraction: NiF ₂ 85.4 wt%, NiO 14.6 wt%											

became larger by the annealing. We did not recognize in the SEM images that the particle size of NiF₂ increased noticeably after the annealing. It might be possible that the conversion reaction could be faster for the particles with enhanced crystallinity due to higher electronic conductivity; however, the relationship between the crystallinity and conversion reactions has not been understood precisely yet. In the previous work regarding FeOF, even though FeOF showed poor crystallinity, it exhibited improved cycling properties over that of pristine FeF₂ [16]. Therefore, it might be difficult to conclude that an improved crystallinity after the annealing has a

strong relationship to the electrochemical properties in the conversion materials. However, this relationship should be studied further in the future.

In addition to X-ray diffraction, XPS was utilized to investigate the formation of a NiO phase on the surface of NiF₂. Fig. 5 shows the O1s, and Ni2p_{3/2} region scans for both NiF₂ and NiO-doped NiF₂. The Ni2p_{3/2} region scans reveal a major peak centered at 858.5 eV for both samples, which is consistent with NiF₂ bonding [27]. The most significant changes are found in the O1s region and in the NiO doped sample an additional peak can be fit from the spectra

**Fig. 5.** X-ray photoelectron spectroscopy graphs of the O1s region and Ni2p region for NiF₂ and NiO-doped NiF₂ materials.

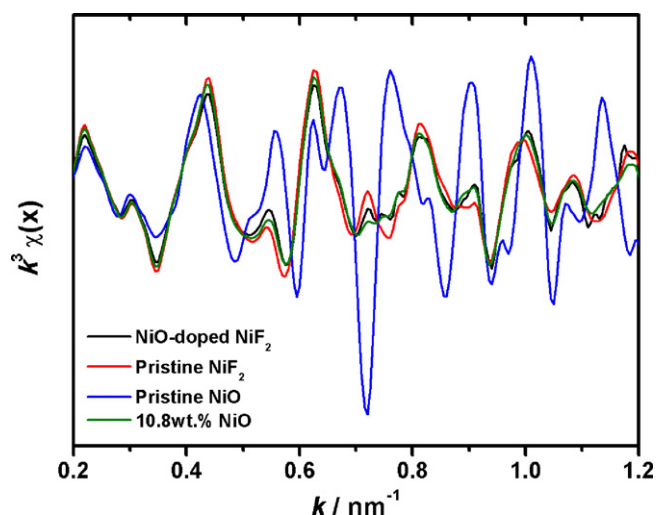


Fig. 6. k^3 -Weighted $\chi(k)$ for nickel K edge EXAFS of NiO-doped NiF_2 electrode, along with NiF_2 and NiO standards and linear combinations of the standards.

(530.2 eV), which is consistent with the formation of a NiO particle [28], revealing that NiO phase presents on the surface of NiF_2 .

Finally, we conducted XAS measurement in order to show strong evidence of presence of NiO. Fig. 6 shows the k^3 -weighted EXAFS spectrum from the initial state of the NiO-doped NiF_2 electrode, fit to a linear combination of spectra using NiF_2 and NiO standards from 0.2 to 1.2 nm^{-1} . The results indicate that the electrode includes approximately 11 ± 4 wt% NiO, which is consistent with the XRD result (see Table 1). Based on XRD, XPS and XAS data, it is confirmed that NiO phase presents both on the surface and bulk. In addition, it is also strongly considered that NiO-doped NiF_2 has NiO-rich surface since XPS detected NiO phase on the surface and the method we utilized is to expose NiF_2 powder in the air and heat. Therefore, it is reasonable to say the NiO doping started from the surface of the powders. We saw an increased amount of NiO by XRD if the oxygen partial pressure is increased during heat treatment.

3.5. Electrochemical properties of NiO-doped NiF_2

Fig. 7 shows the electrochemical profiles for pristine NiF_2 and NiO-doped NiF_2 at room temperature at a 16.15 mA g^{-1} rate. NiO-doped NiF_2 showed slightly better electrochemical properties than

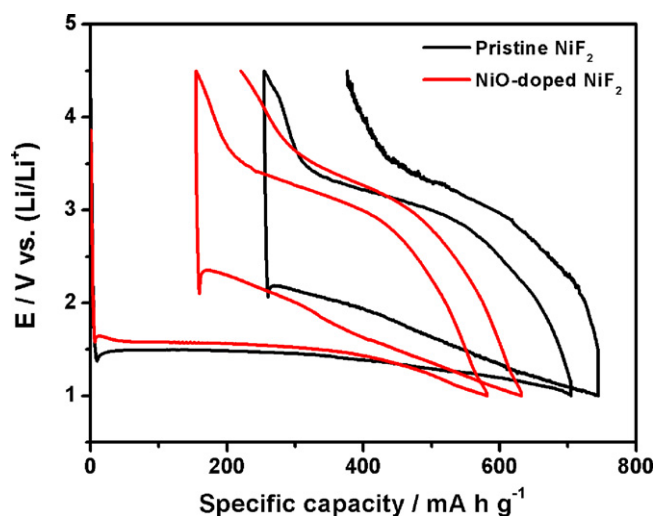


Fig. 7. Electrochemical profiles for NiF_2 and NiO-doped NiF_2 from the 1st discharge to 2nd discharge. Cells were cycled at 16.15 mA g^{-1} at room temperature.

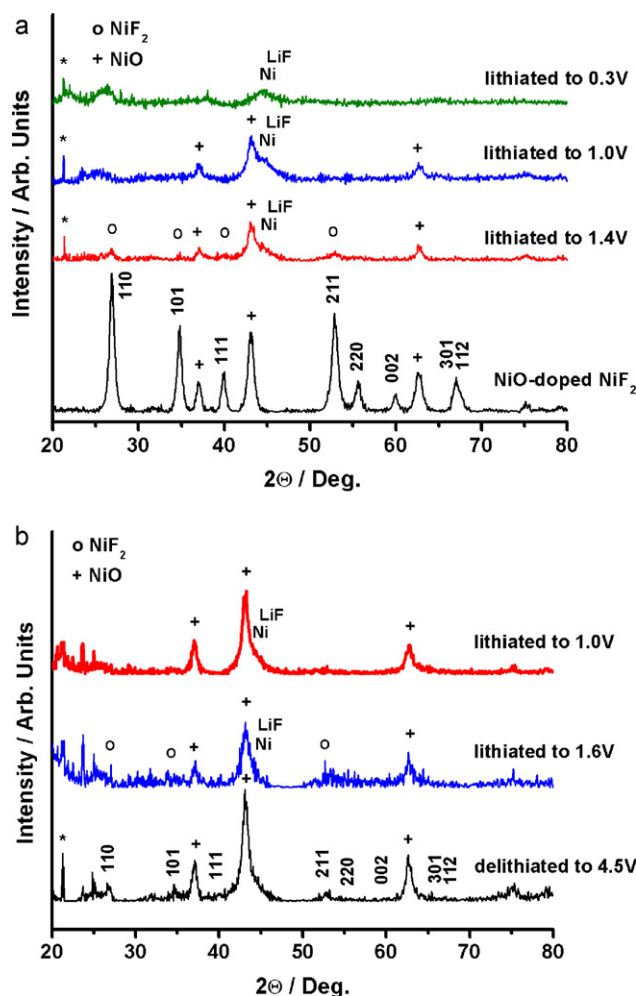


Fig. 8. Ex situ XRD patterns for the (a) 1st lithiation and (b) 2nd lithiation in NiO-doped NiF_2 . (°) Reflections are assigned to NiF_2 and (*) marks impurities related to Li_2CO_3 .

pristine NiF_2 in terms of the conversion potential and reversibility. The conversion potential of NiO-doped NiF_2 was 1.6V, which was 100 mV higher than pristine NiF_2 . This is most likely due to the incorporation of the NiO phase with higher electronic conductivity than that of the highly ionic NiF_2 compound. The initial discharge capacity was lower in NiO-doped NiF_2 by around 17%, since 14–15 wt% of NiO was doped on the surface of NiF_2 . The decreased specific capacity in NiO-doped NiF_2 is in good agreement with the amount of NiO doping estimated by the Rietveld refinement and EXAFS fitting. NiO does not participate in the conversion reaction in the cell potential range from 1.0 to 4.5 V, as it gets converted to Ni and Li_2O under 0.5 V [3]. Compared to pristine NiF_2 , the cell potential dropped much faster after the specific capacity of 400 mA h g^{-1} in NiO-doped NiF_2 at the 1st discharge, indicating that a smaller portion of the SEI layer was involved by some side reactions than in the case of pristine NiF_2 . The reversibility of NiO-doped NiF_2 at the first cycle was $74 \pm 1\%$, which was 10% higher than that of the pristine NiF_2 .

3.6. Structural changes in NiO-doped NiF_2 during the conversion reaction by XRD

Fig. 8 shows the ex situ XRD pattern for the NiO-doped NiF_2 during the conversion reaction. The overall conversion reaction was the same as for the pristine NiF_2 . The Bragg reflections corresponding to NiF_2 disappeared gradually in intensity and simultaneously the

Ni and LiF reflections were developed with the lithiation. As shown in Fig. 8(a), the Bragg reflections assigned to NiF₂ were substantially weakened at 1.4 V and completely disappeared at 1.0 V, indicating that the conversion reaction was terminated. In pristine NiF₂, the conversion reaction still proceeded at 1.0 V, since NiF₂ reflections were clearly observed at 1.0 V. The kinetics of the conversion reaction involving the nucleation and growth of Ni appears to be faster when the NiO phase is present. It is most likely that the NiO phase doped on the NiF₂ reduces the nucleation sites of Ni precipitation and also improves the growth reaction rate of Ni particles, since the M–O covalent bond provides enhanced electronic conductivity compared to the highly ionic M–F bond [15,16,29,30]. There is also the possibility that the NiO phase may enhance the ionic transport through the grain boundaries or act as nucleation centers [31,32]. As shown in Fig. 8(b), although the peaks were broad and weak because of the nanocrystalline structure, NiF₂ phase was regenerated as a consequence of the reversible conversion reaction. The NiF₂ reflections on the XRD patterns were even weaker since the NiO phase in NiF₂ may weaken the reflections further due to partial overlapping of the peaks. The Bragg reflections corresponding to Ni were not clearly detected by the XRD during the 2nd discharge, due to the relatively large signals from NiO and the nanosize line-broadening effect of Ni particles. A better understanding of the phase relationships can be obtained using additional characterizations by magnetic measurement as discussed below.

3.7. Magnetic properties of NiO-doped NiF₂ during the conversion reaction

Fig. 9 shows the magnetic susceptibilities and hysteresis loops for NiO-doped NiF₂. The magnetic susceptibilities (Fig. 9(a)) showed a similar behavior as the pristine NiF₂ (Fig. 3(a)). From Fig. 9(b) and (c), it is also seen that the lithiated NiO-doped NiF₂ also exhibits superparamagnetic behavior at 300 K and ferromagnetic behavior at 5 K, since the phases also included nanosized-Ni particles formed by the conversion reaction. It was observed that lithiated NiO-doped NiF₂ exhibited large magnetic hysteresis at 5 K after the 1st discharge, and the magnetic hysteresis was observed in the 1st charged NiO-doped NiF₂. After the 2nd discharge, the magnetic hysteresis was smaller than the one after the 1st discharge.

4. Discussion

4.1. Formation of Ni nanoparticles during the lithiation in NiF₂ and NiO-doped NiF₂

Based on the ex situ XRD data, it is observed that the NiF₂ Bragg reflections were gradually weakened, while simultaneously the reflections corresponding to Ni and LiF were being developed in both systems. This indicates that two-phase conversion reactions involving the nucleation and growth of Ni and LiF are occurring during the 1st discharge. The conversion reaction terminated at 1.0 V in NiO-doped NiF₂ however, NiF₂ phase still existed at 1.0 V in pristine NiF₂, which suggests that the conversion reaction proceeds faster in NiO-doped NiF₂. As we mentioned in Section 3, differences in the kinetics for the conversion reactions can be mainly ascribed to the higher electronic conductivity of the NiO phase, relative to the NiF₂. However, we cannot rule out the possibilities that the NiO phase may enhance ionic conductivity through the grain boundaries or also act as nucleation centers for nanosized Ni. Fig. 10 shows the schematics illustrating possible reaction mechanisms for the pristine NiF₂ vs. NiO-doped NiF₂ systems. As shown in Fig. 10(b), the NiO phase presents on the surface and in the bulk of the NiF₂ by annealing, which was confirmed by XRD, XPS, and XAS. It enhances the kinetics

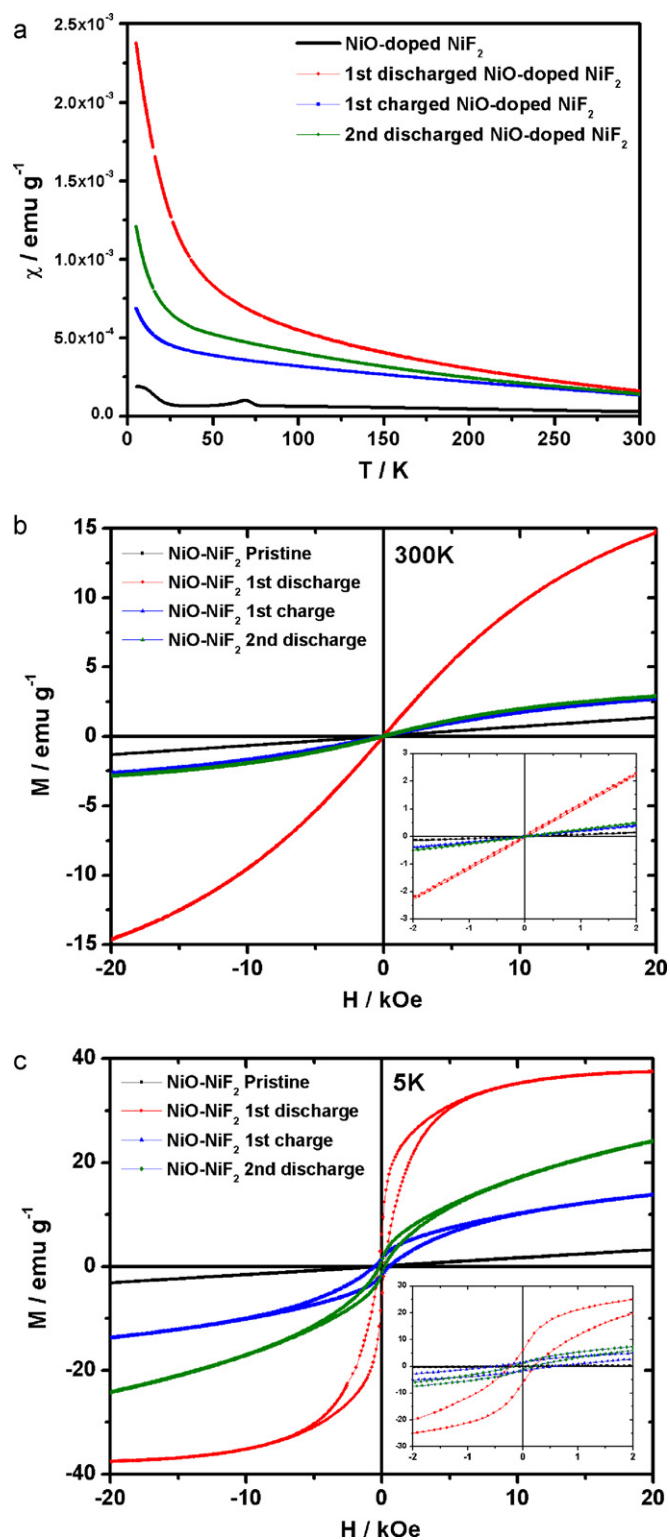


Fig. 9. Magnetic properties for pristine, 1st discharged, 1st charged, and 2nd discharged NiO-doped NiF₂ by SQUID (a) magnetic susceptibilities according to the temperature, (b) magnetic hysteresis loops against the magnetic field (–20 to 20 kOe) at 300 K, and (c) at 5 K. The insets correspond to enlargements of hysteresis loop between –2 kOe and 2 kOe.

of the electron transfer in the reduction reaction from Ni²⁺ to Ni⁰. Table 2 shows the coercivity (H_C) and saturation magnetization (M_S) of both samples at 5 K. The saturation magnetization was obtained by extrapolating the measured high field magnetization vs. the inverse of the applied magnetic field to infinite

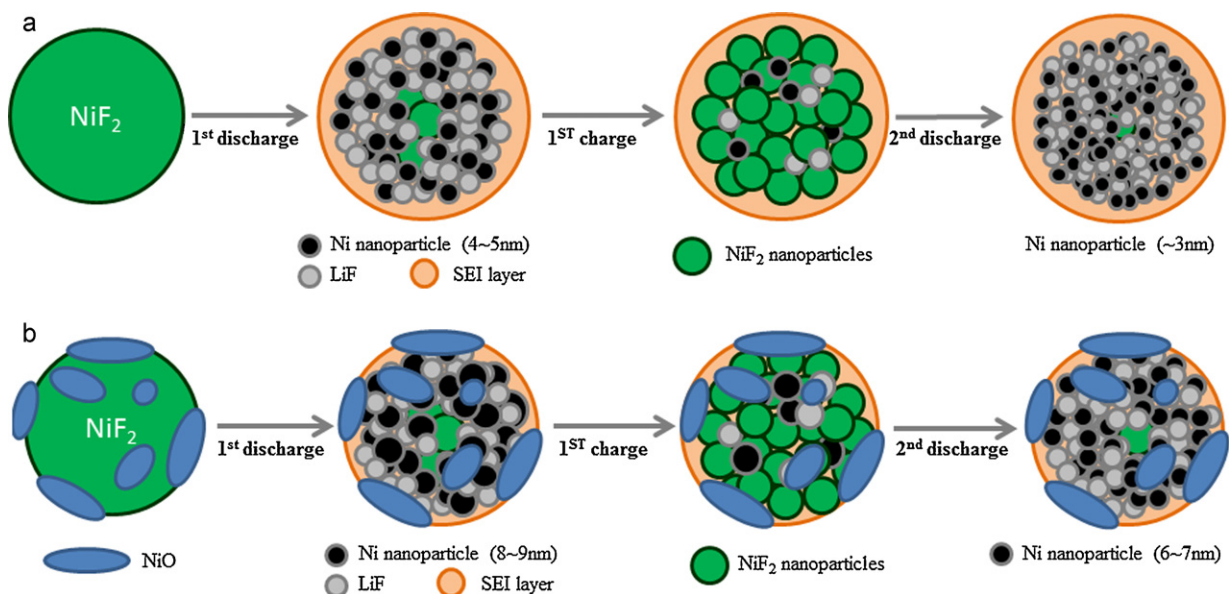


Fig. 10. Schematics illustrating possible reaction mechanisms for (a) pristine NiF₂, and (b) NiO-doped NiF₂.

field [33]. The size of Ni particles was estimated from the previous experimental results [24,34,35]. It was estimated that 4–5 nm sized Ni particles were formed in pristine NiF₂ during the 1st discharge, which is consistent with the value estimated by the XRD analysis. In an earlier study by Yamakawa et al. [23], a solid-state NMR type magnetic measurement was utilized to understand the reaction mechanisms involving nanosized Fe magnetic particles. They found that superparamagnetic nanosized-Fe particles (~3 nm) formed from the FeF₃ by the conversion reaction. Since the kinetics of the conversion reaction was enhanced in the NiO-doped NiF₂ system, a larger particle size of 8–9 nm Ni particles was observed in this system after the 1st discharge. The larger Ni particles with correspondingly less surface area in the NiO-doped NiF₂ system could lead to the reduced amount of SEI layer formation. As a consequence, NiO doping on NiF₂ results in better electrochemical properties in terms of the reversibility. The conversion potential of NiO-doped NiF₂ was 100 mV higher than pristine NiF₂, due to the incorporation of the NiO phase. In earlier research by Li et al. [7], it was observed that the good electronic contact with conductive additives increases the conversion potential in TiF₃ conversion material. In our systems, NiO does not participate in the electrochemical reaction but mainly plays a role as a catalyst to improve the electronic contact between insulating NiF₂ particles. The electrochemical profiles suggest that a larger amount of the SEI layer is formed in pristine NiF₂ because the cell potential curve dropped more slowly in pristine NiF₂. The 1st discharge curve of NiO-doped NiF₂ dropped sharply after the 400 mA h g⁻¹, indicating that a reduced amount of SEI layer is now formed due to enhanced reaction kinetics. We also found improved reversibility of the conversion reaction if the cut-off cell potentials are raised from 0.3 V to 1.0 V. All measurements, including XRD, SQUID and electrochemical cycling, consistently confirmed that larger Ni particles were formed in NiO-doped NiF₂, and as a result, less SEI layer was formed at the 1st discharge.

Table 2

Coercivity (H_C) and saturation magnetization (M_S) at 5 K with zero-field cooling.

Samples	Pristine NiF ₂			NiO-doped NiF ₂		
	$H_{C,ZFC}$ (Oe)	$M_{S,ZFC}$ (emug ⁻¹)	Estimated Ni size (nm)	$H_{C,ZFC}$ (Oe)	$M_{S,ZFC}$ (emug ⁻¹)	Estimated Ni size (nm)
1st discharge	41	18.1	4–5	212	39.9	8–9
2nd discharge		Superparamagnetism		199	31.1	6–7

4.2. Reversibility of the conversion reactions in NiF₂ and NiO-doped NiF₂

It was observed by the ex situ XRD that the initial phases were formed again in both materials by the reversible conversion reactions and there was no signal related to Ni and LiF. With the XRD measurement alone, the conversion reactions in our systems may appear to be completely reversible. However, the magnetic measurements (see Figs. 3(a) and 9(a)) detected some unconverted nanosized-Ni particles in the regenerated NiF₂ and NiO-doped NiF₂, even though there were no noticeable Ni and LiF peaks seen on the XRD patterns. This indicates that the conversion reactions are not completely reversible. As shown in Fig. 10, the size of remaining Ni particles in the fully charged NiO-doped NiF₂ electrode was larger than those in pristine NiF₂, since the magnetic hysteresis was observed in the 1st charged NiO-doped NiF₂ indicating that the unreacted Ni particles were large enough to exhibit the magnetic hysteresis. This can be attributed to larger Ni particles formed at the 1st discharge due to the fast conversion reactions in NiO-doped NiF₂. Therefore, the significant irreversible capacities at the 1st cycle in our systems could possibly be attributed to both the formation of SEI layer during the 1st discharge and irreversibility of the conversion reactions. The reversibility during the 1st cycle was 74% ± 1% in NiO-doped NiF₂, which was 10% higher than the value in pristine NiF₂. It is likely that a smaller amount of SEI layer formed during the 1st discharge may have contributed to the higher reversibility.

4.3. SEI effects on conversion process during the 2nd discharge

In the 2nd discharge, the NiF₂ phase disappeared gradually and XRD peaks corresponding to Ni and LiF were developed in both systems, indicating that the same conversion reactions occur as for the 1st discharge process. As shown in Table 2, magnetic hysteresis measurements indicate that NiO-doped NiF₂ contained larger

nanosized-Ni particles (6–7 nm) after the 2nd discharge. The NiO phase seems to enhance the reaction kinetics at the 2nd cycles, since NiO does not participate in the conversion reactions in the cell potential range from 1.0V to 4.5V. Therefore, NiO phase remains intact during the charge and discharge. It was also observed that Ni particles after the 2nd discharge were smaller than those after the 1st discharge in both systems. We suggest that the electron transfer in the reduction from Ni²⁺ to Ni⁰ is interrupted by the SEI layer formed during the 1st discharge, and therefore the rate of the growth reactions of Ni particles become slower than the 1st discharge. As estimated by the magnetic hysteresis data, the slower reactions lead to smaller Ni particles. The particle size of Ni after the 2nd discharge was decreased by 1–3 nm compared to the size after the 1st discharge in both systems. Using magnetic measurements, we were able to obtain additional structural and phase information related to the conversion mechanism during charge and discharge.

5. Conclusions

The conversion reaction mechanisms of the NiF₂ and NiO-doped NiF₂ from the 1st discharge to 2nd discharge have been investigated using ex situ XRD, SQUID and electrochemical cycling and the structure of NiO-doped NiF₂ has been confirmed by XRD, XPS and XAS. The superparamagnetic, nanosized-Ni particles, which were 4–5 nm and 8–9 nm, were formed as a result of the 1st discharge in pristine NiF₂ and NiO-doped NiF₂, respectively. NiO-doped NiF₂ exhibited slightly higher conversion potential and better reversibility due to the doping of NiO phase, presumably due to the relatively high electronic conductivity. The nucleation sites of Ni were reduced by the presence of the NiO phase in NiF₂ and the kinetics of conversion reaction involving the nucleation and growth of Ni particles was enhanced in NiO-doped NiF₂. Magnetic measurements revealed that larger Ni particles were formed by the conversion reaction in NiO-doped NiF₂. Consequently, a smaller amount of the SEI layer was formed, which allows better reversibility. The conversion reactions were partially reversible in both systems, since small amounts of unconverted nanosized-Ni particles were detected by SQUID in fully charged phases. After the 2nd discharge, the size of Ni particles was even smaller than the one produced by the 1st discharge, indicating that the conversion reactions may be interrupted by the SEI layer. Larger size of Ni particles was also formed in the NiO-doped NiF₂ after the 2nd discharge, which suggested that the kinetics of the conversion reaction was faster during the 2nd discharge, since NiO phase remained unreacted in the cell potential range from 1.0V to 4.5V.

The conversion mechanisms of NiF₂ and NiO-doped NiF₂ are fundamentally similar in the cell potential range of 1.0–4.5V. However, the kinetics of conversion reaction including the nucleation and growth of Ni particles is enhanced by the presence of NiO phase. We suggest that the electronic conductivity of the highly insulating metal fluorides materials was improved by doping of M–O covalent bond by a simple annealing under the partial air atmosphere. In addition, the magnetic measurements provide more fundamental understanding on the phases including nanosized-Ni metal particles during the conversion reactions.

Acknowledgements

This material is based upon work supported as part of the Northeastern Center for Chemical Energy Storage (NECCES), an

Energy Frontier Research Center (EFRC) funded by the US Department of Energy, Office of Science, Office of Basic Energy Sciences under Award Number DE-SC 0001294. The authors acknowledge the assistance in the SQUID (PPMS) measurements by Dr. Eric Fullerton at UCSD. The authors also would like to acknowledge the research supported by ORNL's Shared Research Equipment (SHaRE) User Facility, which is sponsored by the Office of Basic Energy Sciences, US Department of Energy. The authors are grateful for the insightful discussion with Dr. Glenn Amatucci at Rutgers University.

NiO EXAFS data was collected by S. Kelly at the MRCAT beamline of the APS. Use of the APS was supported by the US Department of Energy, Office of Science, Office of Basic Energy Sciences, under Contract No. W-31-109-ENG-38. MRCAT operations are supported by the Department of Energy and the MRCAT Member Institutions.

References

- [1] J.M. Tarascon, M. Armand, *Nature* 414 (2001) 359.
- [2] K. Mizushima, P.C. Jones, P.J. Wiseman, J.B. Goodenough, *Mater. Res. Bull.* 15 (1980) 783.
- [3] P. Poizot, S. Laruelle, S. Grugeon, L. Dupont, J.M. Tarascon, *Nature* 407 (2000) 496.
- [4] A. Deibart, L. Dupont, P. Poizot, J.B. Leriche, J.M. Tarascon, *J. Electrochem. Soc.* 148 (2001) A1266.
- [5] P. Balaya, H. Li, L. Kienle, J. Maier, *Adv. Funct. Mater.* 13 (2003) 621.
- [6] H. Li, G. Richter, J. Maier, *Adv. Mater.* 15 (2003) 736.
- [7] H. Li, P. Balaya, J. Maier, *J. Electrochem. Soc.* 151 (2004) A1878.
- [8] Z.W. Fu, C.L. Li, W.Y. Liu, J. Ma, Y. Wang, Q.Z. Qin, *J. Electrochem. Soc.* 152 (2005) E50.
- [9] Y. Makimura, A. Rougier, J.M. Tarascon, *Appl. Surf. Sci.* 252 (2006) 4587.
- [10] F. Badway, F. Cosandey, N. Pereira, G.G. Amatucci, *J. Electrochem. Soc.* 150 (2003) A1318.
- [11] F. Badway, N. Pereira, F. Cosandey, G.G. Amatucci, *J. Electrochem. Soc.* 150 (2003) A1209.
- [12] F. Badway, A.N. Mansour, N. Pereira, J.F. Al-Sharab, F. Cosandey, I. Plitz, G.G. Amatucci, *Chem. Mater.* 19 (2007) 4129.
- [13] M. Bervas, F. Badway, L.C. Klein, G.G. Amatucci, *Electrochem. Solid-State Lett.* 8 (2005) A179.
- [14] M. Bervas, A.N. Mansour, W.S. Yoon, J.F. Al-Sharab, F. Badway, F. Cosandey, L.C. Klein, G.G. Amatucci, *J. Electrochem. Soc.* 153 (2006) A799.
- [15] I.D. Gocheva, I. Tanaka, T. Doi, S. Okada, J.I. Yamaki, *Electrochem. Commun.* 11 (2009) 1583.
- [16] N. Pereira, F. Badway, M. Wartelsky, S. Gunn, G.G. Amatucci, *J. Electrochem. Soc.* 156 (2009) A407.
- [17] H. Zhang, Y.N. Zhou, Q. Sun, Z.W. Fu, *Solid State Sci.* 10 (2008) 1166.
- [18] G.A. Sawatzky, J.W. Allen, *Phys. Rev. Lett.* 53 (1984) 2339.
- [19] A.C. Pavao, J.P.B.D. Silva, *J. Phys. Chem. Solids* 50 (1989) 669.
- [20] J. Rodriguez-Carvajal, *Physica B* 192 (1993) 55.
- [21] M. Newville, *J. Synchrotron Radiat.* 8 (2001) 322.
- [22] B. Ravel, M. Newville, *J. Synchrotron Radiat.* 12 (2005) 537.
- [23] N. Yamakawa, M. Jiang, B. Key, C.P. Grey, *J. Am. Chem. Soc.* 131 (2009) 10525.
- [24] C.P. Bean, J.D. Livingston, *J. Appl. Phys.* 30 (1959) 120S.
- [25] S. Mitra, K. Mandal, *Mater. Manuf. Process.* 22 (2007) 444.
- [26] A.C. Johnston-Peck, J. Wang, J.B. Tracy, *ACS NANO* 3 (2009) 1077.
- [27] S. Hufner, *Solid State Commun.* 49 (1984) 1177.
- [28] A.R. Gonzalez-Eliphe, J.P. Holgado, R. Alvarez, C. Munuera, *J. Phys. Chem.* 96 (1992) 3080.
- [29] W. Tong, G.G. Amatucci, *Electrochem. Solid-State Lett.* 12 (2009) A219.
- [30] W. Tong, W.S. Yoon, G.G. Amatucci, *J. Power Sources* 195 (2010) 6831.
- [31] J.W. Moon, H.L. Lee, J.D. Kim, G.D. Kim, D.A. Lee, H.W. Lee, *Mater. Lett.* 38 (1999) 214.
- [32] M. Kashiwara, H. Yonetani, S. Suzuki, H. Nakajima, *Mater. Sci. Forum* 658 (2010) 215.
- [33] K.J. Carroll, S. Calvin, T.F. Ekiert, K.M. Unruh, E.E. Carpenter, *Chem. Mater.* 22 (2010) 2175.
- [34] H.E. Schaeferl, H. Kisker, H. Kronmüller, R. Wiirschum, *Nanostruct. Mater.* 1 (1992) 523.
- [35] X. Liua, K. Huanga, S. Zhoua, P. Zhaob, U. Meridorc, A. Frydmanc, A. Gedankenb, *J. Magn. Magn. Mater.* 305 (2006) 504.